

Inverse Hall–Petch relationship in nanocrystalline tantalum

Yizhe Tang^a, Eduardo M. Bringa^b, Marc A. Meyers^{a,*}

^a University of California, San Diego, La Jolla, CA 92093, USA

^b CONICET & Instituto de Ciencias Básicas, Universidad Nacional de Cuyo, Mendoza 5500, Argentina



ARTICLE INFO

Article history:

Received 20 February 2013

Received in revised form

7 May 2013

Accepted 10 May 2013

Available online 17 May 2013

Keywords:

Grain-size effect

Inverse Hall–Petch relationship

Molecular dynamics

BCC metal

ABSTRACT

Tantalum polycrystals (grain sizes varying from 2.5 to 30 nm) generated by Voronoi tessellation were subjected to tension and compression under uniaxial strain loading at strain rates on the order of 10^8 – 10^9 s⁻¹ using molecular dynamics (MD) simulations. In contrast with MD simulations of FCC metals, the response in tension is significantly different from that in compression. In tension, fracture is initiated at grain boundaries perpendicular to the loading direction. It propagates along grain boundaries with limited plastic deformation, at a stress in the range 10–14 GPa. This brittle intergranular failure is a consequence of the high strain rate imposed by MD, leading to a stress that exceeds the grain-boundary cohesive strength. Thus, grain-boundary separation is the principal failure mechanism. In compression, on the other hand, there is considerable plastic deformation within the grains. This occurs at stresses higher than failure in tension. The difference between tensile and compressive response for tantalum is attributed to the difficulty in generating dislocations, in contrast with FCC metals, where tensile failure occurs by void nucleation at grain boundaries associated with partial and perfect dislocation emission. In BCC tantalum, both grain-boundary sliding and dislocation emission are much more difficult.

The compressive yield stress is found to increase with grain size in the 2.5 nm < d < 30 nm region. This inverse Hall–Petch relationship is analyzed in terms of the contributions of dislocation motion and grain-boundary shear to plastic deformation. As the grain size is increased the contribution of grain-boundary sliding is decreased and plastic strain is accommodated by dislocation and motion. In tensile deformation, on the other hand, this behavior is not observed.

© 2013 Elsevier B.V. All rights reserved.

1. Introduction

The plastic response of metals is dictated, in most cases, by shear stresses. The motion of dislocations and generation and propagation of mechanical twins are governed by the resolved shear stress on the slip plane. Thus, the tensile and compressive strengths of polycrystals are the same, if dislocations and twin partials are not shear-direction sensitive, in the absence of crystallographic texture. Indeed, FCC and HCP metals follow the Schmid law fairly closely. In BCC metals, there are instances that lead to tension–compression asymmetry. This phenomenon has been investigated in great depth by Vitek and co-workers [1–6] and Seeger [7] and is attributed to the fact that the dislocation core is not symmetric.

The decrease of flow stress with decreasing grain size (inverse Hall–Petch relationship, also see Ref. [8]), initially identified experimentally by Chokshi et al. [9] in the nanocrystalline regime, was confirmed by MD calculations in FCC metals; it is attributed to the growing role of grain-boundary sliding, since the grain-

boundary surface per unit volume, S_v , is topologically related to the grain diameter, d , through $S_v = 3/d$ (spherical grains assumed to a first approximation [10]). Grain-boundary shear can be taken as proportional to S_v ; thus, one can obtain a relationship between the strain rate and the grain diameter at a constant stress: $\dot{\epsilon} \propto S_v$ or $\dot{\epsilon} \propto 1/d$. Conversely, at a constant strain rate and fixed strain: $\sigma_y \propto d$. Specific detailed analyses, based on more rigorous assumptions, have been developed by Conrad [11], and Argon and Yip [12].

Molecular dynamics simulations of FCC metal deformation have been carried out exhaustively with efforts on dislocation configurations [13–15], plastic deformation [16], grain size effects [8,17,18], and void initiation and growth [19–22]. The potential functions that have had the greatest success in copper are from the embedded atom model (EAM) potential [23] by Mishin et al. [24]. The process of initiation and evolution of plastic deformation is fairly well understood in the nanocrystalline regime. Three mechanisms are found to play pronounced roles: (a) dislocation generation and evolution at grain boundaries; (b) twinning, and (c) grain-boundary sliding. Jarmakani et al. [25] evaluated the contribution of different mechanisms for two grain sizes; the importance of grain-boundary sliding decreased as the grain size increased. Li et al. [26] quantified the contributions of grain boundary and dislocation mechanisms during recovery of nanocrystalline aluminum.

* Corresponding author. Tel.: +1 858 534 4719; fax: +1 858 534 5698.

E-mail addresses: mameyers@UCSD.Edu,
mameyers@mae.ucsd.edu (M.A. Meyers).

Molecular dynamics computations by Schiøtz and Jacobsen [27] first predicted a negative Hall–Petch slope for Cu in the nanocrystalline domain. Additionally, work by Vo et al. [28] and Koslowski et al. [29] showed that the energetics of grain boundaries also play an important role in the strength of nanocrystals. Dongare et al. [30] studied the ductile failure and spallation of nanocrystalline Cu [31] by MD for a mean size of 6 nm.

However, BCC metals have not been subjected to the same number of investigations. The main reason is the difficulty of implementing proper potential functions. The EAM potential for tantalum has been developed by Guellil and Adams [32]. More recently, the Finnis–Sinclair potential [33,34] as it has been implemented by Dai et al. [35] has also been used. This has enabled an improved understanding of void growth in tantalum, studied by Rudd [36] and Tang et al. [37,38].

The principal goal of our study is to apply the methodology of molecular dynamics to gain an improved understanding of polycrystalline plasticity in BCC metals. Tantalum was chosen as a model material because of its excellent ductility in the polycrystalline regime. Indeed, total tensile elongations of $\sim 40\%$ at 298 K and $\sim 25\%$ at 78 K are routinely observed [39]. Additionally, the tension–compression asymmetry experimentally observed does not take place for tantalum at temperatures equal to and above ambient temperature and this contribution can be ignored.

There are only a limited number of MD studies on polycrystalline BCC metals, mostly focusing on deformation and fracture mechanisms. Latapie and Farkas [40] investigated the fracture behavior of nanocrystalline α -Fe samples containing mode I cracks, with grain sizes varying from 6 to 12 nm. Both intragranular and intergranular fracture were observed. The fracture resistance was found to be grain-size dependent and there exists a “most brittle” grain size [41]. Frederiksen et al. [42] studied the plastic deformation of nanocrystalline molybdenum sample containing 16 grains, with a grain size of 12 nm, subject to tensile loading. The plastic deformation was found to be mainly accommodated by formation of grain-boundary cracks, even at an increased temperature of 1000 K. Rudd [43] simulated high-rate plastic deformation of nanocrystalline Ta sample subjected to uniaxial and biaxial compression, using a Finnis–Sinclair potential [33,34]. The nanocrystalline sample was generated by solidification of liquid Ta system and had a relatively wide range of grain sizes, between 10 nm and 20 nm, 10–20 nm. A new quaternion method was proposed to determine the local environment of each atom, i.e. atomic orientation, and both dislocations and twins were observed. Investigations of grain-size effects in BCC nanocrystalline metals were conducted using MD simulations only for α -Fe and Ta. Recently Jeon et al. [44] reported MD simulation results in uniaxial tension of nanocrystalline Fe samples containing 16 grains, with grain sizes varying from 3.7 to 19.7 nm. An inverse Hall–Petch relationship between flow stress, which was averaged over a plastic strain interval of 0–4%, and grain size was observed when grain sizes were smaller than the critical grain size 14.7 nm; while the peak stress exhibited inverse Hall–Petch relationship within the whole grain-size range studied. The break-down of Hall–Petch for the averaged flow stress was found to be due to the transition of deformation mechanism from dislocation activity to grain-boundary activity when grain sizes were smaller than 14.7 nm. MD simulations of uniaxial tension of nanocrystalline Ta samples containing 16 grains, with grain sizes varying from 3.25 to 12.99, were conducted by Pan et al. [45]. The flow stress at 5% strain and the peak stress were found to decrease with decreasing grain size, exhibiting an inverse Hall–Petch relationship. Strain-rate and temperature effects were also studied. Dislocation activity, grain-boundary activity, as well as local BCC to FCC and HCP phase transformation were observed. However, in these Ta simulations, the yielding strains were $\sim 0.1\%$, and the strains at which

maximum stresses occurred were ~ 0.2 , beyond, somewhat, the strain at plastic flow within conventional deformation.

The computational investigation whose results are presented here had two principal objectives: (a) to establish the deformation mechanisms in a polycrystalline BCC metal in both tension and compression, and (b) to investigate whether an anomalous flow-stress–grain-size relationship is observed in the nanocrystalline regime and to determine/estimate the critical grain size at which a Hall–Petch relationship transits to inverse Hall–Petch relationship. The regime accessible by molecular dynamics is ideally suited for the investigation of nanocrystalline metals.

2. Computational methods

MD simulations were carried out using LAMMPS [46] with the Extended Finnis–Sinclair potential [35] which gives correct elastic constants at zero pressure and reproduces the pressure dependence of specific volume up to values of close to 500 GPa [47]. In the current work the pressure did not exceed 60 GPa; thus the potential is very robust under the applied stresses.

Polycrystalline Ta samples were generated by Voronoi tessellation, with periodic boundary conditions in all directions. The polycrystalline specimens used in tension simulations had a constant box size $200 \times 200 \times 200$ unit cells with grains ranging from 3.15 to 27.3 nm ($N_{\text{sample}} = 16 \times 10^6$ atoms). The limitation in the upper limit of the grain size is due to the number of atoms contained in the volume ($V = (66 \text{ nm})^3$) and the requirement for a minimum number of grains to represent a polycrystalline aggregate. For compressive deformation, the same topological structures with 68 grains were used; the grain size was varied from 2.5 (cubic, $L = 8.25 \text{ nm}$) to 30 nm (cubic, $L = 99 \text{ nm}$, $N_{\text{sample}} = 54 \times 10^6$ atoms). Simulations were carried out in a number of computer

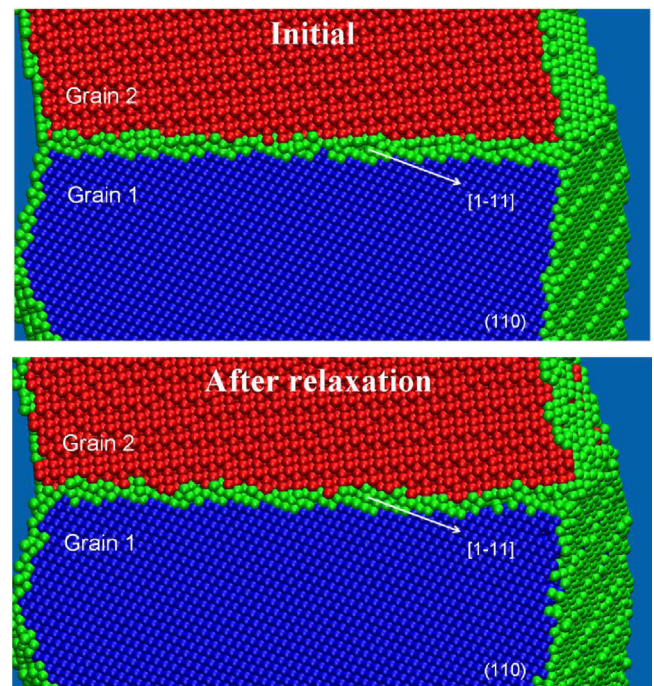


Fig. 1. Side views showing the atomic arrangement near a grain boundary before and after relaxation. Only two adjacent grains were isolated from a 15 nm grain-sized sample. Blue and red atoms are from neighboring grains (BCC), and green atoms are non-BCC atoms. After relaxation there is a “sharpening” of the boundary visible through a decrease in the number of green atoms. GB structure includes some [1–11]-oriented segments. (For interpretation of the references to color in this figure legend, the reader is referred to the web version of this article.)

systems, from single core workstations, to the TeraGrid Super-computer, using 512 cores.

The samples were equilibrated using conjugate gradient (CG) minimization and then thermalized at 300 K for 10 ps; however there is no thermostating during loading to capture possible plastic heating effects. NVE integration was used with time steps of 1–2 fs. The Common Neighbor Analysis (CNA) [48] filter was used to reveal the defects generated by plastic deformation and VMD [49] was used for visualization. The computations were conducted at strain rates of 10^8 s^{-1} in tension and 10^9 s^{-1} in compression.

In the Voronoi tessellation used to generate the nanocrystalline structure, the grain orientation distribution is totally random,

representing a non-textured bulk polycrystal. We used energy minimization and equilibration at constant temperature (300 K) and zero pressure to relax the original grain-boundary structure, although we understand that annealing at an elevated temperature would increase grain boundary relaxation, albeit increasing average grain size. After relaxation, the grain-boundary structure did not change noticeably, and no ledges, steps or special grain boundaries were observed. Fig. 1 shows the grain-boundary structure before and after relaxation, for a particular grain boundary. In this case, after relaxation there is a slight ‘sharpening’ of the boundary.

However, another reason that might limit grain boundary changes is that periodic boundary conditions and relatively low

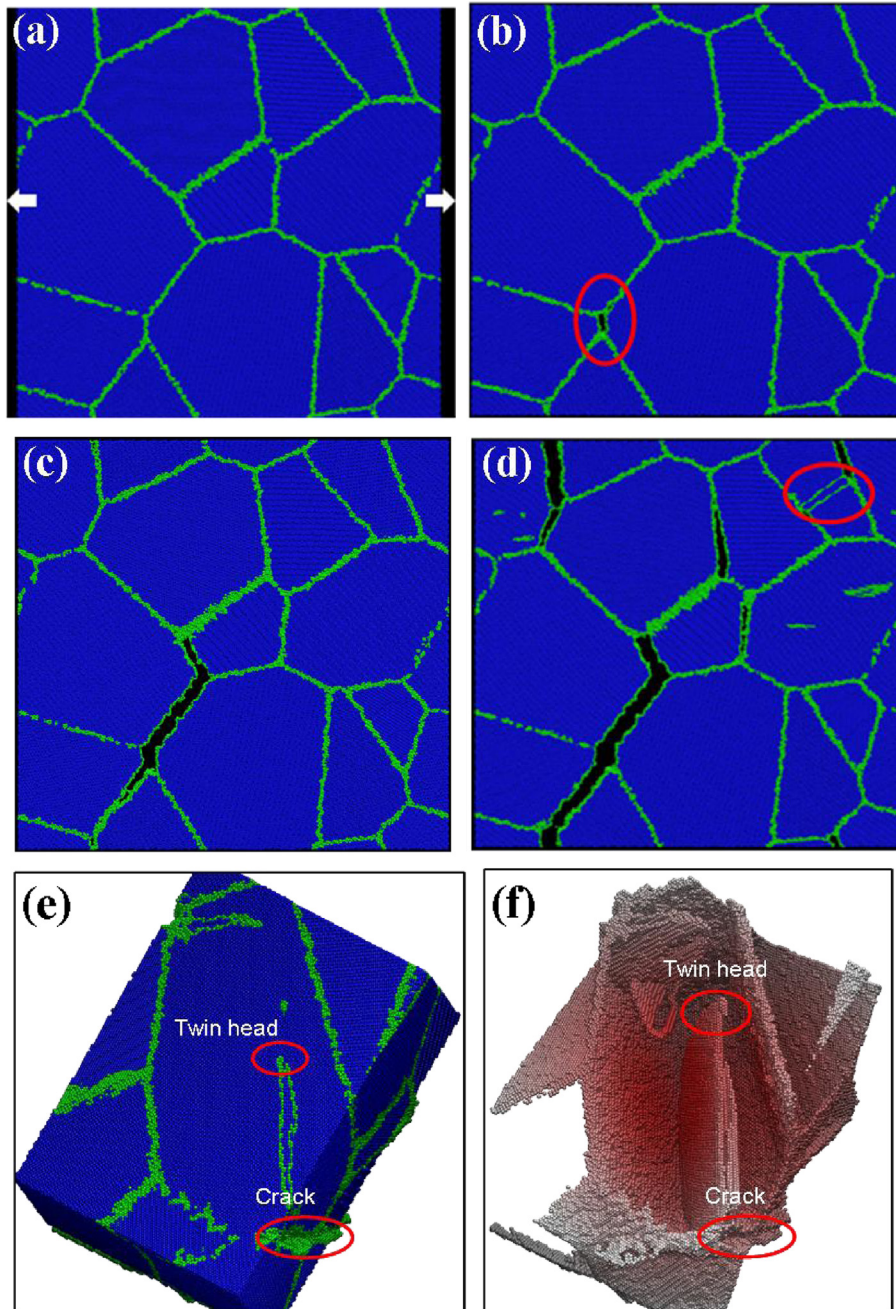


Fig. 2. Plastic deformation and failure evolution of a polycrystal with 273 nm grain size under uniaxial tensile strain (strain rate of 10^8 s^{-1} , direction of traction marked in a); (a) $\epsilon=0$, $\sigma=0$; (b) $\epsilon=5\%$, $\sigma=11.2 \text{ GPa}$; (c) $\epsilon=5.25\%$, $\sigma=9.30 \text{ GPa}$; (d) $\epsilon=5.5\%$, $\sigma=3.74 \text{ GPa}$. Blue atoms are BCC atoms and green atoms are non-BCC. Twin is marked by red circle in (d). Crack-induced twinning is shown in (e) for $\epsilon=5.25\%$ and the corresponding defect structure (non-BCC atoms) is shown (f). Note that the twin head, which is thinner, moves away from the crack, as marked by red circles in (e) and (f). (For interpretation of the references to color in this figure legend, the reader is referred to the web version of this article.)

temperature (300 K) could prevent ledges, steps and special grain boundaries from forming. These structures typically evolve with grain growth, which is not relevant in this paper, where we focus on plasticity at a particular mean grain size. Voronoi tessellation is a standard procedure used in most nanocrystalline simulations of 3D grains. Comparison with experimentally observed grain-boundary structures for nanocrystals is complex, since the experimental grain-boundary structure is not necessarily an equilibrium structure, and it is largely determined by grain-growth dynamics, which cannot be addressed by Voronoi tessellation itself.

The structure of grain boundaries in metals has been studied experimentally, analytically, and computationally (e.g., Murr [50], Gleiter [51], Sutton and Balluffi [52]). Dislocation/disclination models, coincidence site models, polyhedral models, and the Displacement Shift Complete (DSC) lattice are some of the approaches implemented to grapple this complex problem with five macroscopic degrees of freedom. The structure and energy of each boundary depend on these five variables and others. For instance, in FCC metals, when the stacking fault is low, the majority of the boundaries after some grain growth are 'special' boundaries, which have a lower mobility than random grain boundaries and have significantly lower free energy. However, grain boundary distributions might be different for nanoscale grains and Wolf and co-workers [53–55] devoted great effort to the computational modeling of grain boundaries in both FCC and BCC metals.

As another example, Rohrer et al. [56] report that the incidence of special grain boundaries $\Sigma 3$ and $\Sigma 9$ dominates the population of grain boundaries in Ni after some growth. This is what led Holm et al. [57] to choose Al in computations of the grain boundary energy in order to obtain comparison with experimental results for different grain boundary configurations. Interestingly, experimental results by

Voehringer [58] on Cu, and Meyers and McCowan [59] on Ni show that the number of twins/grain increases significantly with grain growth: from 1.1 to 2.6 when grain size increases from 10 to 550 μm in Cu, and from 0.27 to 1.72 when grain size increases from 7.6 to 120 μm in Ni. This is corroborated at the nanoscale by MD simulations conducted by Farkas et al. [60] showing that the number of twins/grain increased from 0.1 to 0.9 when Cu was 'annealed' and the grain size increased from 5 to 8 nm. Sputtered copper subjected to in situ annealing and TEM observation [61] showed likewise an increase in twins/grain from 0 to 1 when the grain size was increased from ~ 50 to ~ 270 nm. These results are a clear demonstration that the grain boundaries change with grain growth. Regretfully, similarly detailed studies for BCC metals like Ta are scarcer than studies for FCC metals, but the role of grain growth is also expected to be important in the grain boundary type distribution. In this study we focus on the mechanical behavior of a non-textured sample, with grains below 100 nm, and grain growth does not play a role for the established conditions.

3. Results and discussion

3.1. Grain size effects in tension

Fig. 2 shows the sequence of damage propagation for a grain size of 27.3 nm. There is no obvious dislocation activity observed. Failure initiates preferentially at boundaries normal to the traction application direction and then continues along boundaries at an angle with it. Separation of a normal boundary is circled in Fig. 2b whereas the propagation of the crack by extension is shown in Fig. 2c. There are also instances where twinning and dislocation generation are associated with (or following) the formation of

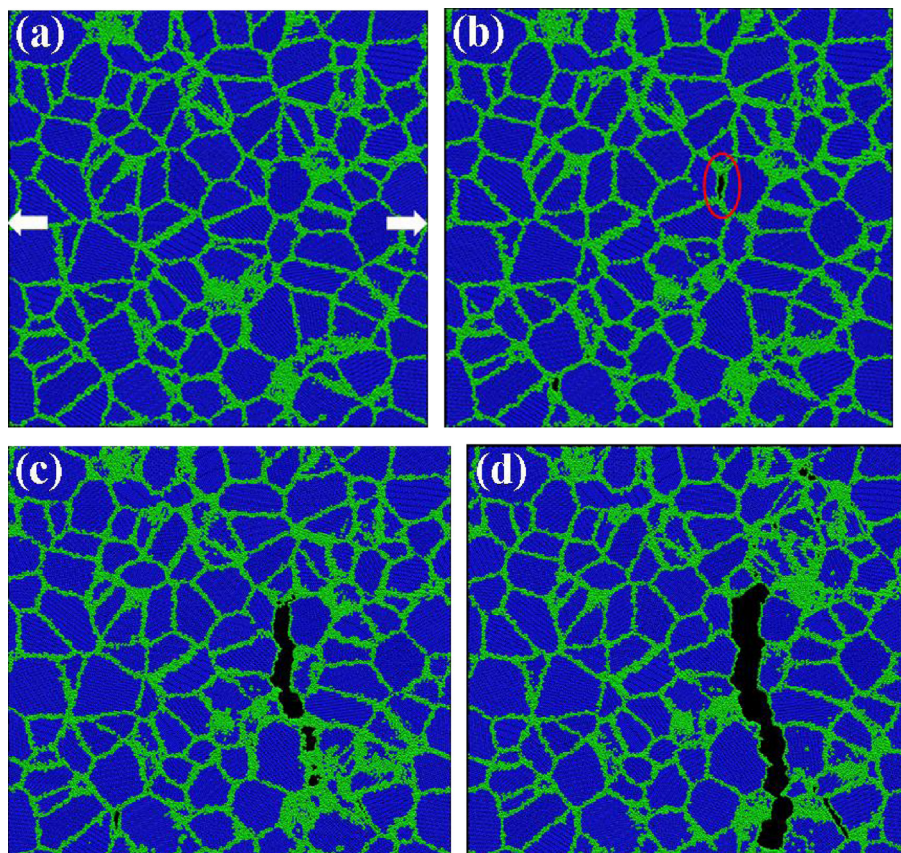


Fig. 3. Plastic deformation and failure evolution of a polycrystal with 8.2 nm grain size under uniaxial tensile strain (strain rate of 10^8 s^{-1}); (a) $\epsilon=0$, $\sigma=0$; (b) $\epsilon=6.5\%$, $\sigma=12.2 \text{ GPa}$; (c) $\epsilon=6.75\%$, $\sigma=4.56 \text{ GPa}$; (d) $\epsilon=7\%$, $\sigma=1.97 \text{ GPa}$.

grain-boundary cracks. One such event circled in Fig. 2e and f shows twinning followed by a crack and propagating away from the crack. The twin formed at the cracked grain boundary has the same morphology as that formed at the free surface of a void [62], and the propagating direction of the twin can be recognized by identifying the position of the twin head (thinner part of the twin, as circled in Fig. 2f). Obviously the two phenomena are connected. Crack formation by shear stress concentration at grain boundaries due to dislocation pile-up or twinning is known as the Zener–Stroh [63,64] mechanism in the metallurgical literature.

Reducing the grain size to 8.2 nm did not change the mechanisms of failure initiation and propagation. The sequence for an 8.2 nm grain size is shown in Fig. 3. The first crack opening is circled in Fig. 3b; the same sequence occurs. There is only limited dislocation activity, with failure propagating by openings along the grain boundaries. Grain-boundary separation takes place with minor plastic deformation. The normal stress at which the separation onset takes place, 12.2 GPa ($\epsilon=6.6\%$) is slightly larger than for grain size $d=27.3$ nm: $\sigma=11.2$ GPa ($\epsilon=5.25\%$).

Schematic representations of the two failure mechanisms are shown in Fig. 4a and b (for grain-boundary crack initiation and propagation) and c and d (for cracking and associated twinning). The stresses at which these events occur are grain-size dependent.

These results are similar to the MD simulation of BCC nanocrystalline molybdenum [42] and are surprisingly different from earlier calculations for FCC copper [65]. In copper, there was extensive stacking-fault emission from selected grain-boundary regions, leading to the initiation of voids, which then grew along the boundaries and eventually coalesced. The early growth process in FCC copper was associated with profuse dislocation emission into the grains.

Using MD simulations, Zhang et al. [66] observed twinning-induced cracking in columnar nanocrystalline molybdenum sample containing four grains. The occurrence of twinning before cracking in this case is probably due to the lack of grain boundaries which are normal to the tensile loading direction. They used hexagonal grains and a loading direction parallel to two sides of the hexagon, and the

selected crystallographic orientations (hexagon with axis in $\langle 110 \rangle$ direction) ease twinning in grains with higher Schmid factor (see Fig. 1d by Zhang et al. [66]; 30° and 60° grains have twins but 0° and 90° grains with zero Schmid factor do not).

Fig. 5 shows the principal failure initiation mechanisms observed for polycrystalline tungsten subjected to compressive loading in a Hopkinson pressure bar [67]. Although the grain size and strain rate regimes are radically different from the simulations, the phenomena observed have considerable similarity. Both twinning and cracking are observed and are indicated by numbers in the figure. There is a definite correlation between the two phenomena. The numbers indicate the events: 1: crack at twin–twin intersection; 2: crack at twin–grain-boundary intersection; 3: crack within twin; 4: crack at twin extremities. This response has been attributed to the competition among three principal mechanisms: slip, twinning, and grain-boundary cleavage, each with its own constitutive response. The high strain rate sensitivity in BCC metals is the direct result of the small activation volume. Hence, high strain rates will favor mechanisms that have lower strain-rate sensitivity. It was hypothesized [67,68] that this was the case for grain-boundary separation in tungsten, and the molecular dynamics simulations corroborate this.

In support of the MD predictions are the experimental results obtained in high-strain-rate deformation ($\sim 10^7$ s $^{-1}$) of vanadium in uniaxial strain [69]. There was significant fracture, with fractures propagated along the grain boundaries, in accordance with the suggestion made here, that the flow stress exceeds grain-boundary cohesion at high strain rates. These experiments also revealed that monocrystals had a higher tensile strength than polycrystals, in contrast with H–P predictions and in accordance with competing deformation mechanisms having different regions of dominance.

Fig. 6 shows the normal stress along the loading direction and von Mises stress vs. strain curves for different specimens. There is clear grain-size dependence, the maximum normal stress (a measure of strength) increasing with decreasing grain size; while the maximum von Mises stress decreasing with decreasing grain

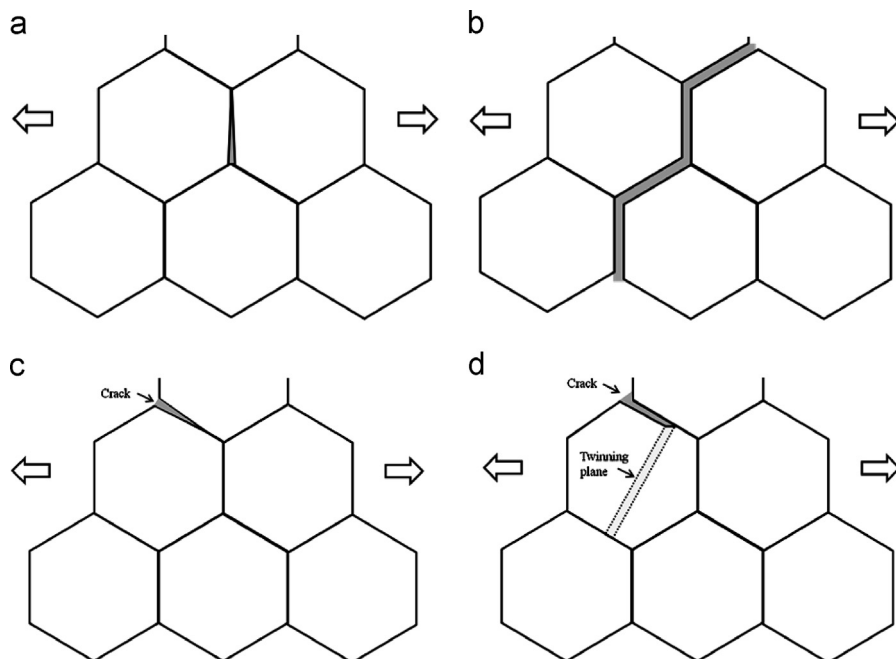


Fig. 4. Schematic representation of principal mechanisms identified for the failure of nanocrystalline tantalum in tension (a and b) grain-boundary separation starting at a boundary normal to traction application direction; (c and d) grain-boundary separation associated with twinning in a Zener–Stroh mode (crack induced twinning).

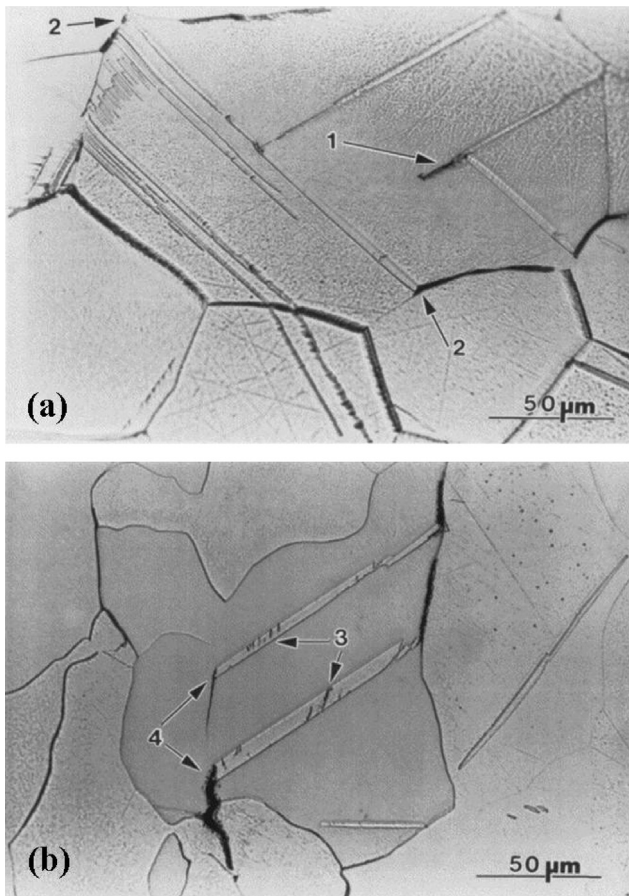


Fig. 5. Twinning and cracking in high-strain rate compressive plastic deformation of polycrystalline tungsten; 1: Crack at twin-twin intersection; 2: crack at twin-grain-boundary intersection; 3: crack within twin; 4: crack at twin extremities (from Dümmer et al. [67], Fig. 7, p. 6277).

size (inverse Hall–Petch relationship). The grain size dependence of the strength (maximum normal tensile stress) and the maximum von Mises stress is shown in Fig. 7. The inverse Hall–Petch relationship of maximum von Mises stress is a result of the increasing grain-boundary to volume ratio and grain-boundary related plasticity with decreasing grain size. This is consistent with MD predictions for FCC metals [13,70], in which enhanced grain-boundary sliding and an inverse Hall–Petch slope were produced below a critical grain size, but differs from that in the deformation and fracture mechanisms. In BCC tantalum, plasticity and decohesion of grain boundaries occurred without assistance of dislocation activity; whereas profuse dislocations were observed in FCC metals.

The grain-size dependence of the maximum tensile normal stress in the molecular dynamics simulations is thought to be connected to two factors:

- The size dependence of cohesive grain-boundary strength. This is analogous to the classic problem of a rope, whose strength decreases with its length. This behavior can be represented by Weibull statistics. The problem is best posed as: if a grain boundary with length l_1 has a distribution of strengths, what is the distribution of strengths of a boundary with length $l_2 = Nl_1$?
- As the grain size is decreased, grain rotation, involving grain-boundary sliding, becomes more prevalent. Thus, the stress concentration at grain boundaries is accommodated by grain-boundary activity. As seen in Fig. 6b, the von Mises stress for small grain sizes is considerably lower than that for large ones.

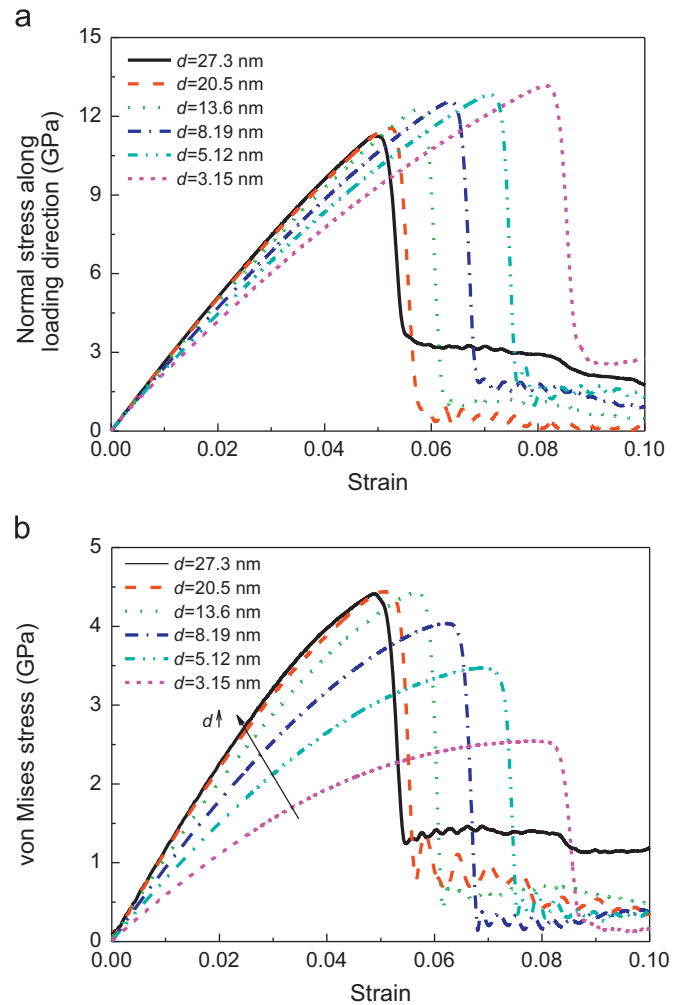


Fig. 6. Stress–strain curves ((a) normal and (b) von Mises stresses) for nanocrystals with different grain sizes under uniaxial tensile strain (strain rate of 10^8 s^{-1}).

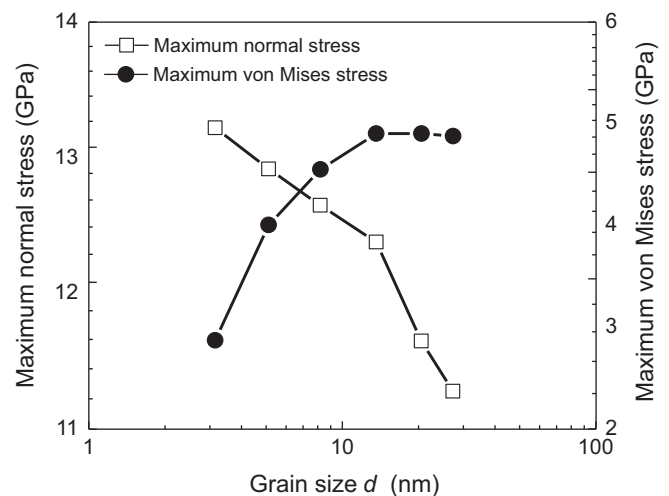


Fig. 7. Maximum normal stress and von Mises stress as a function of grain size d under uniaxial tensile strain (strain rate of 10^8 s^{-1}).

Thus, the onset of decohesion is delayed, resulting in a higher cohesive strength of grain boundaries.

The decohesion of grain boundaries is a typical brittle fracture phenomenon in metals. This happens when the material has a

high resistance to plastic deformation, grain boundaries are weak; this is accentuated when the temperature is low and/or strain rate is high. In the computations, even when the temperature was increased to 1000 K, this decohesion phenomenon was still observed, as shown in Figs. 8 and 9, indicating that the flow stress was still higher than the grain boundary cohesive strength. There is a significant increase in thermal agitation with increasing temperature T , shown in Fig. 8 through the increased fraction of atoms in light color; Fig. 9 shows the effects of temperature, direction of loading, and strain rate on the mechanical response. We note that temperature is assumed to play an important role during plastic deformation of BCC metal, related to the temperature-dependent dislocation mobility. For the nanocrystals simulated here dislocations do not play any role, even in grain with experimentally achievable grain sizes, and temperature effects are only related to GB decohesion.

3.2. Grain size effects in compression

In compression, the tensile stresses acting normally to the boundaries are considerably reduced and therefore reaching the cohesive strength requires much higher applied stresses. These stresses have been calculated by Ashby and Hallam [71], and Hori and Nemat-Nasser [72]. Thus, the deformation and failure mechanisms can be very different from tension. As seen in Fig. 10, nanocrystalline tantalum undergoes large strain (0.18) without grain-boundary separation. Filtering of the atoms with CNA reveals the dislocation pattern. Plasticity (dislocations and twins as seen in Fig. 11) is initiated from grain boundaries at a von Mises stress considerably higher than in tension (6 GPa for $d=30$ nm in compression vs. 4 GPa for $d=273$ nm in tension). It should be noted that these values are much larger than the ones encountered in high-strain-rate experiments by Wei et al. [73]: the flow stress of

nanocrystalline Ta with average grain size of ~ 40 nm in compression was 1–2 GPa. This is due to the much higher strain rates and smaller grain sizes in the MD computations. For the smaller grain size (7.5 nm), only a few dislocations are observed (Fig. 11a), whereas a much larger number of dislocations are found in the sample with the largest grain-size (30 nm) (Fig. 11b). A few twins are also found in the largest grain sized sample (Fig. 11b). It will be shown in Section 3.2.1 that the contributions of grain-boundary sliding and dislocation movement are grain-size dependent.

The normal stress along the loading direction and von Mises stress vs. strain curves for different grain sizes are shown in Fig. 12a and b, respectively. There is a clear grain-size dependence, as shown in Fig. 12b. The maximum von Mises stresses, and the von Mises stresses at strains of 5%, 15% and 18% decrease with decreasing grain size. This behavior (inverse Hall–Petch relationship), shown in Fig. 13, is also observed in MD simulations of FCC nanocrystalline metals but typically occurs below a critical grain size (15–20 nm for Cu) [27] which is much smaller than in the present case (> 35 nm). In contrast with tensile deformation, the grain-size dependence of the von Mises stress in compression is directly related to plasticity, including both grain-boundary sliding and dislocation motion.

3.2.1. Dislocation activity: dislocation density analysis

In this section the contributions of the different mechanisms to the total strain will be extracted for different grain sizes. One can consider the total shear strain γ_t as composed of three components

$$\gamma_t = \gamma_e + \gamma_d + \gamma_{Gb}, \quad (1)$$

where γ_e is the elastic strain, γ_d is the contribution from dislocations and γ_{Gb} is the contribution from grain boundary sliding.

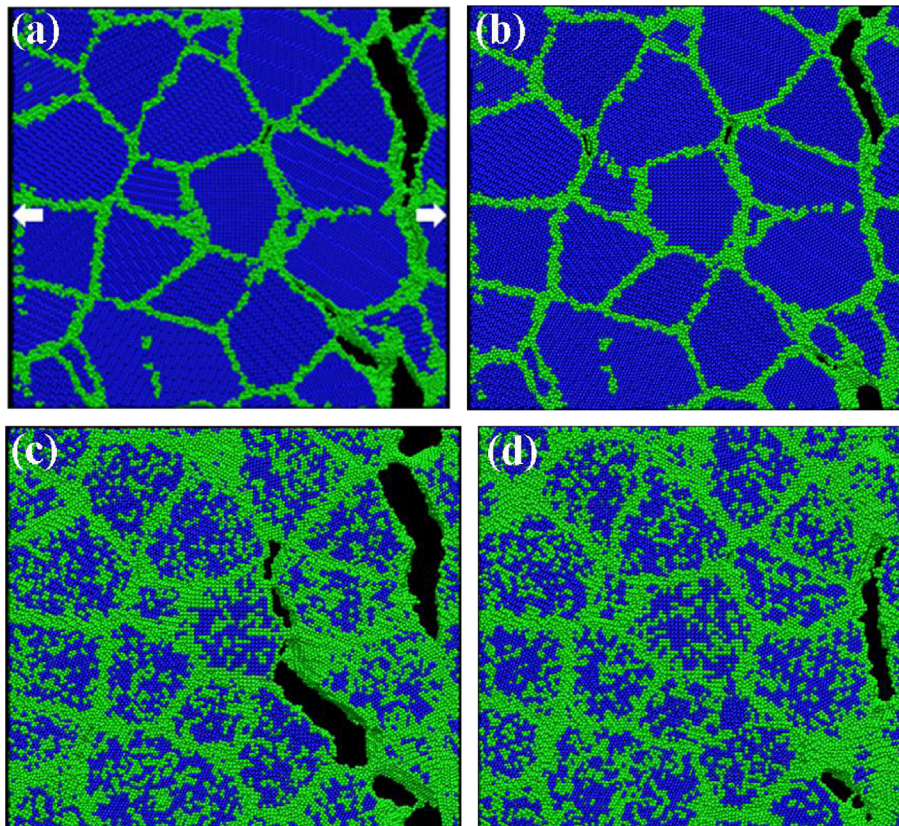


Fig. 8. Effect of temperature on fracture of a 10 nm grain size sample under uniaxial tensile strain at a strain rate of 10^9 s $^{-1}$ (a) $T=10$ K, $\epsilon=8.67\%$; (b) $T=300$ K, $\epsilon=8\%$; (c) $T=1000$ K, $\epsilon=12\%$; and at 10^8 s $^{-1}$ (d) $T=1000$ K, $\epsilon=6.58\%$.

The Orowan equation is, in the absence of an orientation term M

$$\gamma_d = \rho l b, \tag{2}$$

where ρ is the dislocation density, l is the distance that the dislocation moves (we assume $l \approx d$) and $b=0.286$ nm is the Burgers vector. The density ρ can be expressed as

$$\rho = \frac{nd}{d^3} = \frac{n}{d^2} \tag{3}$$

where n is the total number of dislocations in a grain with diameter d . Thus, n can be expressed through Eqs. (2) and (3)

$$n = \frac{\gamma_d d}{b} \tag{4}$$

From Eq. (4), one can see that the total number of dislocations per grain at a specified plastic shear strain is proportional to the grain size d , if no grain boundary shear takes place. Alternatively, at a specified dislocation density ρ , the total number of dislocations n is proportional to d^2 .

According to the Orowan equation (Eq. (2)), one should expect a decrease in ρ with increasing d

$$\rho = \frac{\gamma_d}{bd} \tag{5}$$

The dislocation density ρ , assuming that the plastic deformation $\gamma_t - \gamma_e$ is totally accommodated by dislocation movement (i.e. $\gamma_t - \gamma_e = \gamma_d$), can be calculated from Eq. (5). To obtain the plastic shear strain γ_d from the von Mises stress–uniaxial strain curve (Fig. 12b), elastic unloading is assumed to subtract the elastic shear strain γ_e from the total shear strain γ_t . It should be pointed out that, for uniaxial strain, the von Mises stress is twice the shear stress and the uniaxial strain is numerically equal to the shear strain γ_t . For $d=7.5, 10, 15,$ and 30 nm, the values for γ_d obtained at a uniaxial strain of 0.18 ($\gamma_t=0.18$) are, 0.133, 0.131, 0.135 and 0.140, respectively. The corresponding values for the required dislocation density ρ (assuming no grain-boundary shear) obtained from Eq. (5) are $6.20, 4.58, 3.15$ and $1.63 \times 10^{16} \text{ m}^{-2}$, respectively. Fig. 14 shows the decrease in dislocation density with increasing grain size if all plastic deformation is accommodated by dislocation generation and motion. The dislocation density is proportional to $1/d$.

If plastic deformation also occurs by grain-boundary activity, the required dislocation density will deviate from the calculated values above ($\sim 1/d$). In order to quantitatively determine the actual contribution of dislocations to plastic deformation for different d , the dislocation density was calculated directly from the atomistic simulation results using the algorithm and software tool DXA developed by Stukowski and Albe [74]. It is noted that the calculated dislocation density also includes contributions of

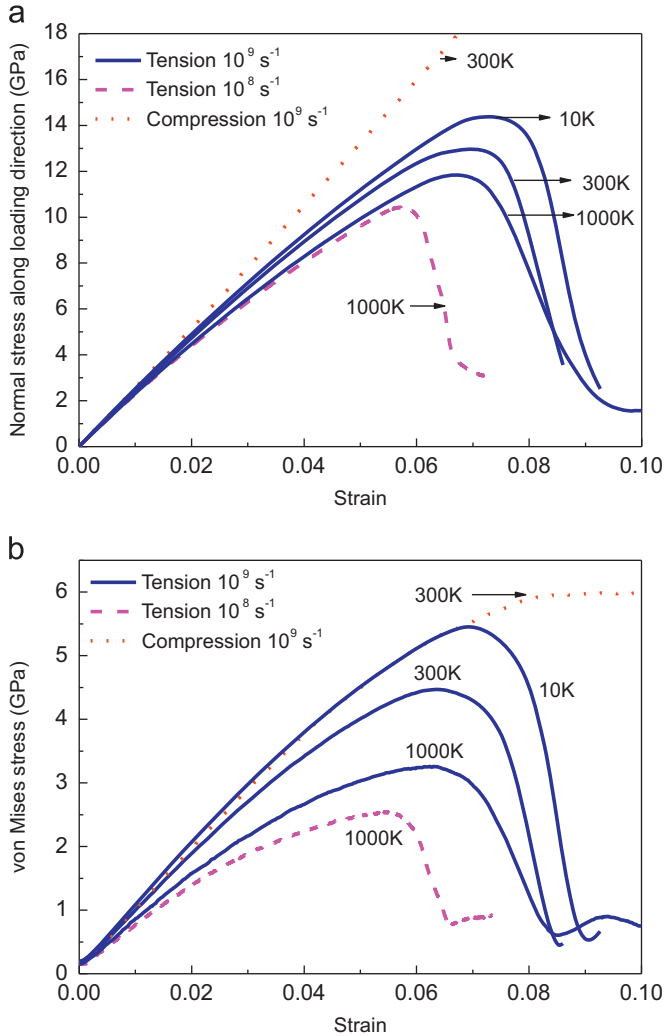


Fig. 9. Stress–strain curves ((a) normal and (b) von Mises stresses) for nanocrystal with 10 nm grain size under different loadings (uniaxial tensile and compressive strain, strain rate, temperature).

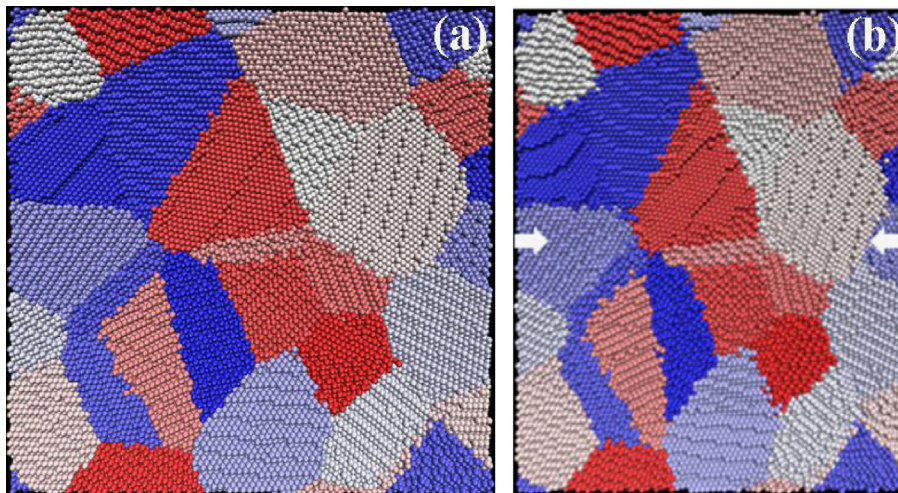


Fig. 10. (a) Initial ($\epsilon=0$) and (b) after deformation ($\epsilon=18\%$) images of a polycrystal with 7.5 nm grain size under uniaxial compressive strain (strain rate of 10^9 s^{-1}). Loading direction is horizontal, and different grains are colored by different colors. (For interpretation of the references to color in this figure legend, the reader is referred to the web version of this article.)

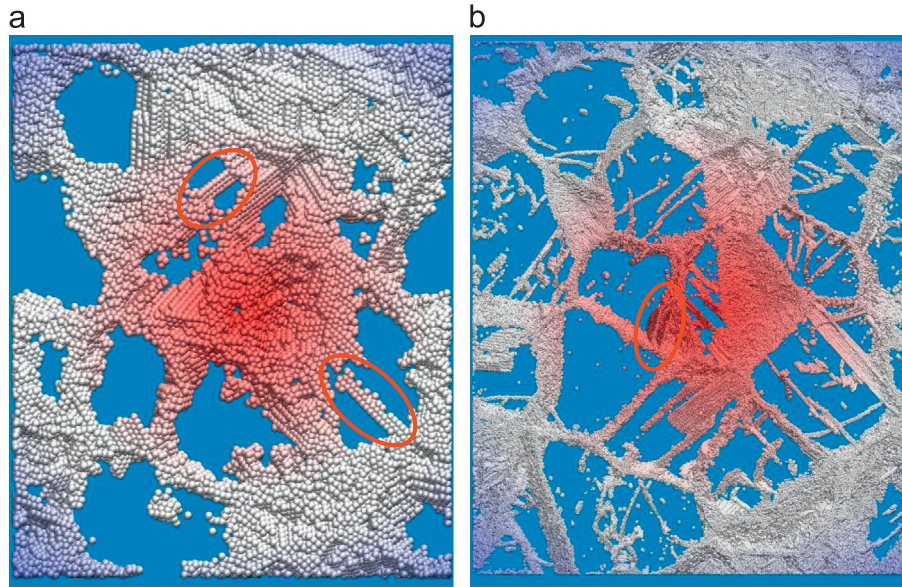


Fig. 11. Defects identified by CNA in polycrystals with small and large grain sizes under uniaxial compressive strain (strain rate of 10^9 s^{-1}). (a) $d=7.5 \text{ nm}$, $\epsilon=18\%$, $\sigma=52.7 \text{ GPa}$; dislocations are circled. (b) $d=30 \text{ nm}$, $\epsilon=18\%$, $\sigma=50 \text{ GPa}$, twin is circled. The number of dislocations is much larger in sample with 30 nm grain size than that with 7.5 nm grain size.

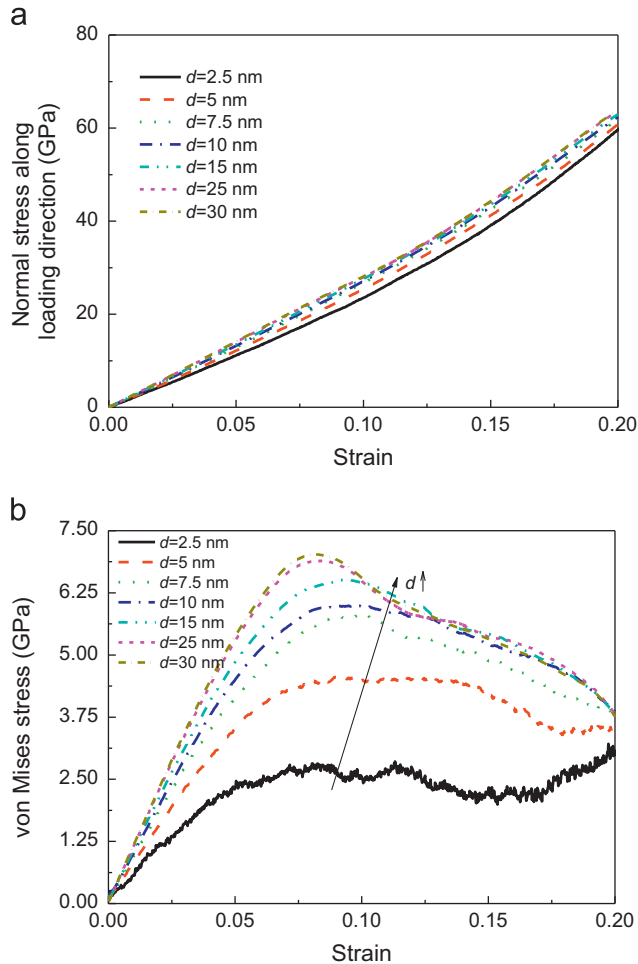


Fig. 12. Stress–strain curves ((a) normal and (b) von Mises stresses) for nanocrystals with different grain sizes (2.5–30 nm) under uniaxial compressive strain (strain rate of 10^9 s^{-1}).

grain-boundary dislocations, which are not involved in dislocation plasticity. The fraction of these grain-boundary dislocations could be noticeable, especially for small grain sizes. Therefore, the initial

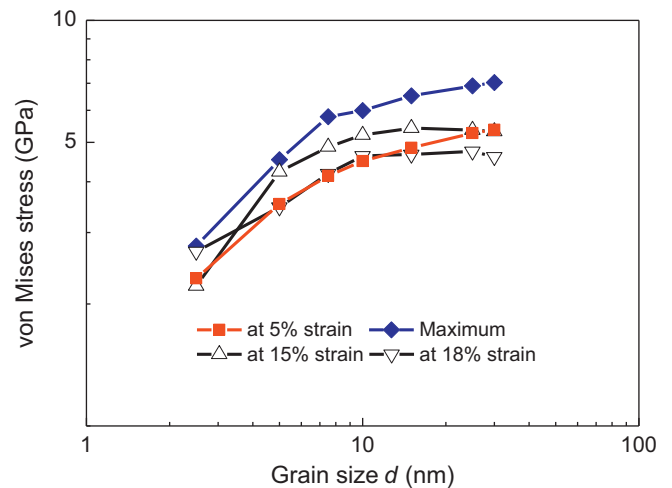


Fig. 13. Maximum, 5%, 15% and 18% von Mises stress as a function of grain size d under uniaxial compressive strain (inverse Hall–Petch behavior); notice decrease in slope as d increases (strain rate of 10^9 s^{-1}). (For interpretation of the references to color in this figure, the reader is referred to the web version of this article.)

dislocation density (at $\epsilon=0$) is subtracted from the calculated total dislocation density to eliminate the contributions of grain boundary-dislocations, given the fact that density of grain boundary-dislocations would not change much during deformation. Fig. 15 shows the calculated dislocation density ρ after subtraction as a function of total strain for different grain sizes d . The dislocation densities for grain sizes of 7.5, 10, 15 and 30 nm are almost at the same level up to a strain of 0.18. At a total strain of 0.18, the dislocation densities for different grain sizes $d=7.5, 10, 15,$ and 30 nm are $2.76, 2.44, 2.63$ and $2.3 \times 10^{16} \text{ m}^{-2}$, respectively. For comparison, they are also plotted in Fig. 14 (red line). The grain size dependence of ρ is significantly lower than if all plastic deformation were accommodated by dislocation slip. Thus, another deformation mechanism has to operate: grain-boundary shear.

The results computed from Eq. (5) are only approximate, since we assume that the dislocation displacement is equal to d , when in reality it is a fraction of it ($l < d$ in Eq. (2)). Additionally,

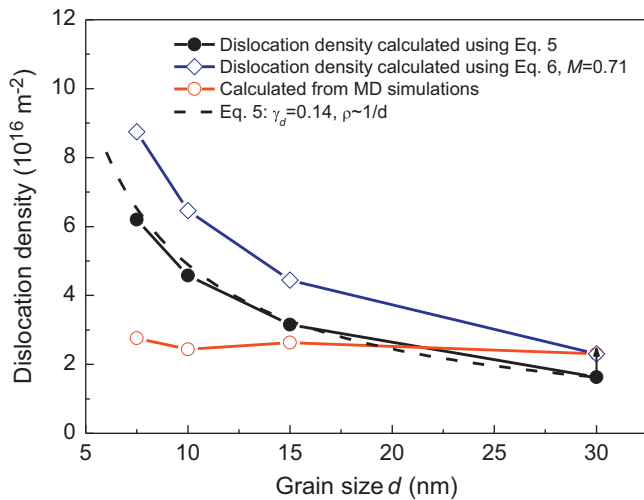


Fig. 14. Dislocation density (at a uniaxial strain of 0.18) as a function of grain size from both Orowan equation (Eqs. (5) and (6), black and blue curves, and Eq. (5) when γ_d is a constant 0.14, black dash curve) and from MD predictions (red curve, uniaxial compressive strain, strain rate of 10^9 s^{-1}). Orowan-based densities for accommodation of plastic strains $\gamma_c - \gamma_e$ are nearly proportional to grain size $1/d$; calibration used a correction $M=0.71$ to account for orientation effects and deviation of dislocation mean-free-path l from d . Role of grain-boundary shear, decreases with increasing grain size d . (For interpretation of the references to color in this figure legend, the reader is referred to the web version of this article.)

dislocations move in more than one slip plane and this introduces an orientation factor. These effects are grouped under the same parameter M which is used in the normalization.

$$\gamma_d = M\rho b d \quad (6)$$

The factor $M=0.71$ was used in obtaining the normalized curve, which is shown for comparison in Fig. 14 (blue line). It is very clear that, for grain sizes smaller than 30 nm, the plastic deformation is accommodated by both dislocation motion and grain boundary shear. The curves approach each other as the grain size is increased, showing that the contribution of grain boundary shear decreases as the grain size d is increased.

Thus, we conclude that the increase in von Mises stresses with increasing grain size (inverse Hall–Petch relationship) in Fig. 13 is the result of the transition of deformation mechanisms from grain-boundary sliding to dislocation movement when d increases. For the small grain sizes, grain-boundary involved plasticity is easier to occur, due to both the small size and the large grain boundary to volume ratio, which leads to a lower shear stress (von Mises stress). As the grain size increases, it is more difficult for grain-boundary involved plasticity to occur, and the shear stress increases until emission of dislocations from grain boundaries dominates the deformation and reduces the shear stress.

3.2.2. Grain boundary activity: displacement field analysis

In order to quantitatively evaluate the role of grain boundaries during compressive deformation of nanocrystals, the displacement field of the sample was calculated to identify the operating deformation mechanisms. A linear displacement field along the loading direction, corresponding to the uniform strain field, was subtracted from the full displacement field to eliminate the constant part of the displacement gradient and to represent its nonuniformity. Although the residual displacement field (deviation from linear field) is not exactly identical to plastic deformation, it is directly related to it, and thus is a good representation. Plastic deformation is difficult to be quantitatively defined and represented at the atomic scale.

Fig. 16a shows the residual displacement field (deviation from linear field) for $d=5$ nm. Large deviations always occur for grain boundary atoms, while the atoms in the grain interiors preferentially stay at their reference positions (linear field or uniform strain). This can be attributed to the elastic compatibility effect. Several deformation mechanisms involved can be identified: (a) grain boundary migration (atoms located at both sides of a grain boundary move in the same direction, normally to the grain boundary), (b) grain boundary diffusion (atoms located in one side of a grain boundary move through the grain boundary into the neighboring grain) and (c) grain boundary sliding (atoms located at both sides of a grain boundary move in opposite directions parallel to the grain boundary). For a particular grain, sliding of different grain boundaries in the same clockwise/counterclockwise direction leads to grain rotation, as shown in Fig. 16b, and sliding in different clockwise/counterclockwise directions leads to grain shear. As seen in Fig. 16c, the grain is elongated in the horizontal direction by shear. Another way to show grain rotation is through atomic images. As seen in Fig. 17a and b, an isolated grain is shown, and rotation is observed by comparing the orientation change (marked by yellow arrows in Fig. 17a and b) after deformation. However, it is also possible that this orientation change is only contributed by the uniform compressive strain. From the residual displacement field, in which the contribution of uniform strain is already eliminated, now it is clear that there is indeed grain rotation induced by grain boundary sliding, as shown in Fig. 17c.

Fig. 18 shows the residual displacement field for $d=15$ nm and the corresponding atomic image. It is found that, for some grains, only the grain boundaries undergo large plastic deformation, while the interior has small residual displacement and there are no defect generated, as shown in the grain marked as “1” in Fig. 18a and b. This is similar to the 5 nm grain size. However, in some other grains, nearly-uniform large residual displacements can be found for some part of the interior, which is the result of shearing of the grain, as shown in the grain marked as “2” in Fig. 18a. Dislocations or twins may be generated by such shear deformation, which is consistent with the fact that there are many more dislocations in the interior of larger grains, as seen in Fig. 11b. Actually, two twins are found in the grain marked as “2”, as shown in Fig. 18b. It is worthy to point out that displacements for a larger grain size d_1 are somewhat larger than that for a smaller grain size d_2 ; however, if the displacements are scaled by the ratio of grain size d_1/d_2 , they will be smaller.

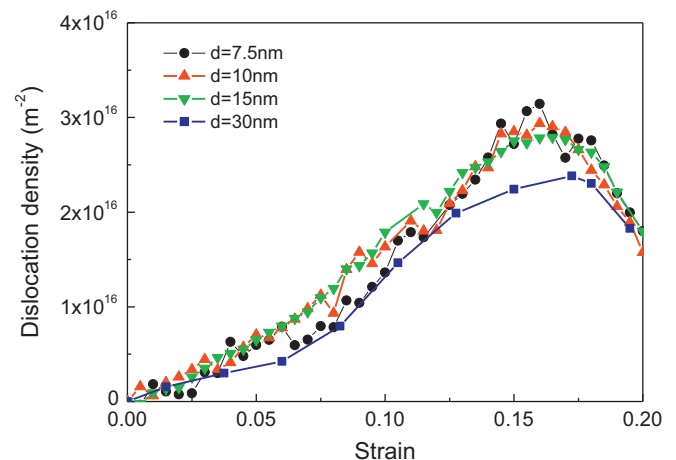


Fig. 15. Dislocation density as a function of strain under uniaxial compressive strain (strain rate of 10^9 s^{-1}); dislocation densities up to 20% are almost at the same level for $d=7.5, 10, 15$ and 30 nm.

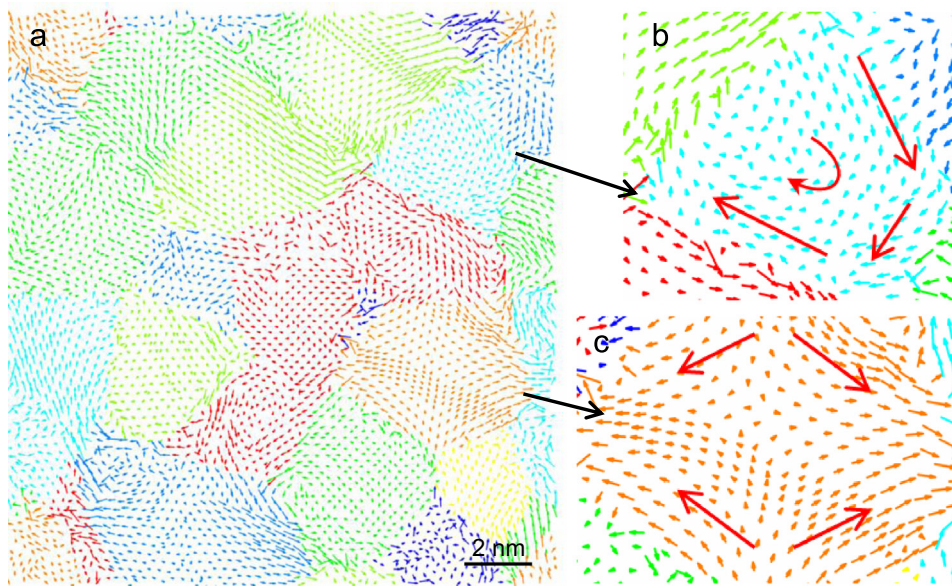


Fig. 16. (a) Residual displacement field (in-plane) for sample with 5 nm grain size under uniaxial compressive strain ($\epsilon=18\%$, strain rate of 10^9 s^{-1} , only a slice, $0 < z < 0.3 \text{ nm}$ is shown, different colors indicate different grains); (b) rotation and (c) elongation of grains in x direction by grain boundary sliding. (For interpretation of the references to color in this figure legend, the reader is referred to the web version of this article.)

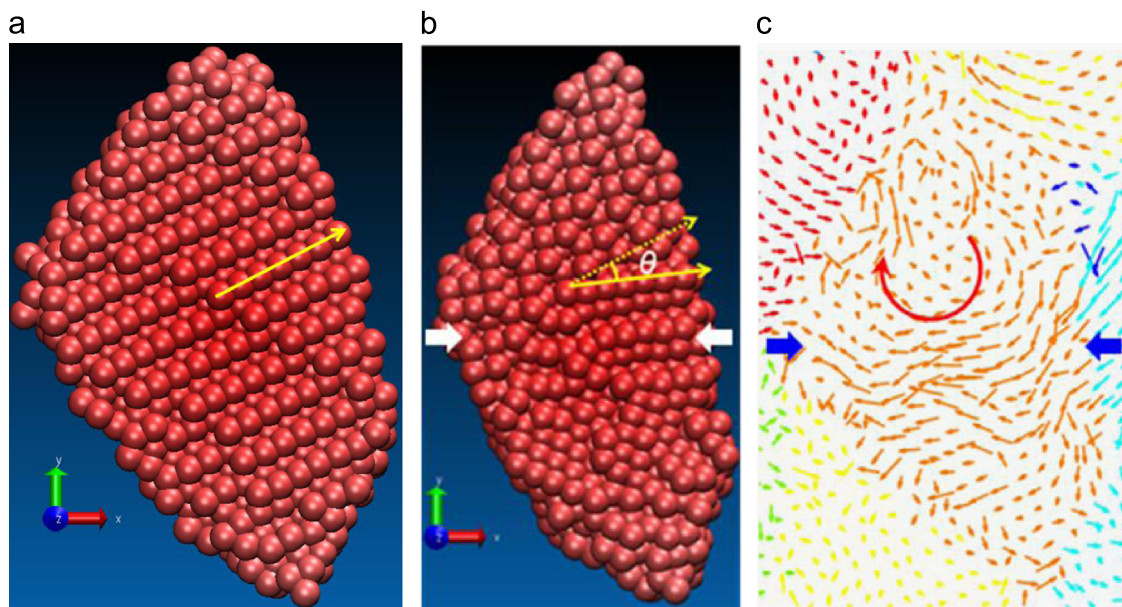


Fig. 17. Initial and deformed images of a representative grain in sample with small grain size ($d=5 \text{ nm}$) under uniaxial compressive strain (strain rate of 10^9 s^{-1}). Loading direction is horizontal. Difference in orientations marked by yellow arrows in (a) $\epsilon=0\%$ and (b) $\epsilon=18\%$ indicate grain rotation ($\theta=18\%$ during deformation); (c) residual displacement field showing grain rotation ($\epsilon=18\%$). (For interpretation of the references to color in this figure legend, the reader is referred to the web version of this article.)

4. Conclusions

Nanocrystalline tantalum behaves differently in tension and compression. In tension, decohesion of grain boundaries occurs before plasticity due to the high flow stress at the imposed strain rate ($\sim 10^8 \text{ s}^{-1}$) which exceeds the grain-boundary cohesive strength. This is a direct consequence of the high Peierls–Nabarro (P–N) stress in BCC metals, which is responsible for their high strain-rate sensitivity. Grain-boundary decohesion and plastic flow are competing processes and, as the strain rate increases, the flow stress increases and will eventually exceed the grain-boundary decohesion stress. This leads to the occurrence of intergranular brittle fracture at high strain rates.

In compression, plasticity occurs in the form of both grain boundary sliding and dislocation activity, Deformation is accommodated primarily by grain boundary activity for the smaller grain sizes, and by dislocation generation and motion for larger grain sizes. A transition from grain-boundary plasticity to dislocation plasticity is starting for grain sizes larger than 20 nm.

It is observed that the maximum von Mises stress increases with increasing grain size from 2.5 to 30 nm. An inverse dependence of flow stress on grain size was obtained in compression. This is due to the decreasing role played by grain-boundary shear as the grain size is increased. We quantitatively estimate the contributions of plastic deformation by dislocation motion and grain-boundary shear for the grain sizes (2.5–30 nm) investigated.

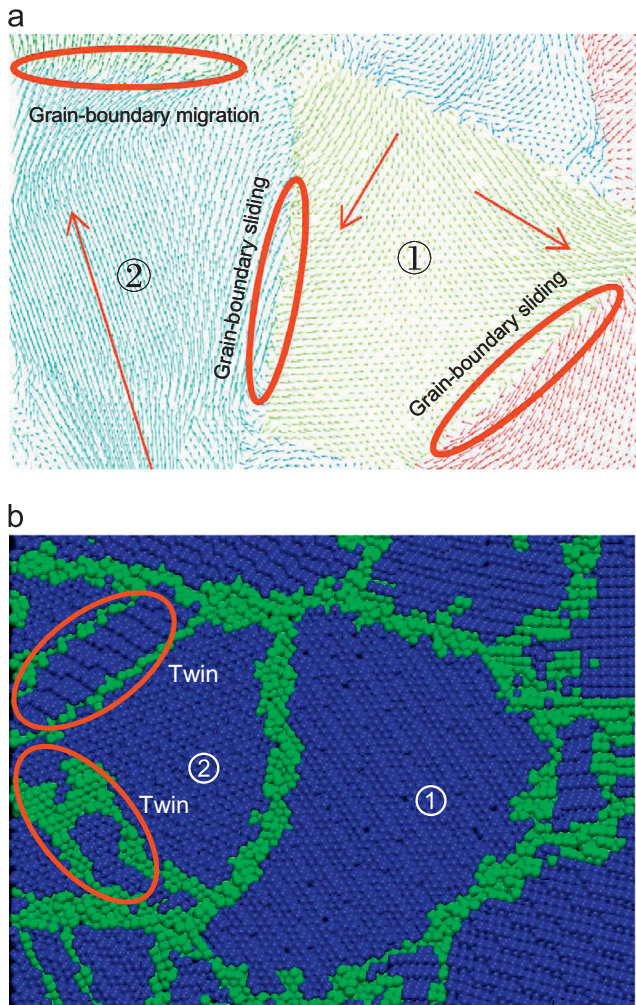


Fig. 18. (a) Residual displacement field (in-plane) for 15 nm grain size sample under uniaxial compressive strain ($\epsilon=18\%$, strain rate of 10^9 s^{-1} , only a slice, $0 < z < 0.3 \text{ nm}$ is shown, coloring is according to grain orientation). For grain 1 (green), similar to 5 nm grain case, only grain boundaries undergo large plastic deformation (mostly sliding), the interior has small residual displacements; for grain 2 (light blue), besides grain boundaries (migration and sliding), interior also has large plastic deformation, which is a result of shear of the whole grain, generating dislocations or twins; (b) the corresponding atomic image showing no defects generated in grain 1 and two twins (marked by red circles) generated in grain 2. (For interpretation of the references to color in this figure legend, the reader is referred to the web version of this article.)

The mechanisms of grain-boundary sliding are identified through the tracking of the flux of atoms.

Grain boundary configurations modeled in this simulation study are not necessarily the same as the ones obtained experimentally, since experimental grain structures depend strongly on detailed nanocrystal synthesis conditions, often including grain growth due to annealing. When grain growth is involved, grain size effects might not only be due to scale, but also to possible changes in grain boundary nature. Here we isolate the scale effect, and focus on mechanical properties for a given average grain size at the nanoscale.

Acknowledgments

This research was funded by the University of California Research Laboratory Program and was supported in part by the

National Science Foundation through TeraGrid resources provided by TACC Ranger under grant number TG-DMR060050. Helpful discussions with Drs. T. Germann, C. Brandl, A. Caro at LANL and Dr. R. Rudd at LLNL are gratefully acknowledged. Mr. C. Ruestes' help with the dislocation density calculation is also acknowledged. E.M.B. thanks computer time at the SUMO cluster at the Centro Atómico Bariloche, at the TWISTER cluster at the Instituto Tecnológico Universitario in Mendoza, and funding from PICT2008-1325.

References

- [1] M.S. Duesbery, V. Vitek, *Acta Mater.* 46 (1998) 1481–1492.
- [2] R. Gröger, A.G. Bailey, V. Vitek, *Acta Mater.* 56 (2008) 5401–5411.
- [3] R. Gröger, V. Racherla, J.L. Bassani, V. Vitek, *Acta Mater.* 56 (2008) 5412–5425.
- [4] R. Gröger, V. Vitek, *Philos. Mag.* 89 (2009) 3163–3178.
- [5] R. Gröger, V. Vitek, *Acta Mater.* 56 (2008) 5426–5439.
- [6] V. Vitek, V. Paidar, in: J. Hirth (Ed.), *Dislocations in Solids Volume 14: A Tribute to F.R.N. Nabarro*, Elsevier, Amsterdam, Holland, 2008, pp. 439–514.
- [7] A. Seeger, *Z. Metallkd.* 93 (2002) 760–777.
- [8] M.A. Meyers, A. Mishra, D.J. Benson, *Prog. Mater. Sci.* 51 (2006) 527–556.
- [9] A.H. Chokshi, A. Rosen, J. Karch, H. Gleiter, *Scr. Metall.* 23 (1989) 1679.
- [10] M.A. Meyers, K.K. Chawla, *Mechanical Metallurgy: Principles and Applications*, Prentice-Hall, Inc., New Jersey, 1997.
- [11] H. Conrad, *Metall. Mater. Trans. A* 35A (2004) 2681–2695.
- [12] A.S. Argon, S. Yip, *Philos. Mag. Lett.* 86 (2006) 713–720.
- [13] E.M. Bringa, A. Caro, Y.M. Wang, M. Victoria, J.M. McNaney, B.A. Remington, R.F. Smith, B.R. Torralva, H. Van Swygenhoven, *Science* 309 (2005) 1838–1841.
- [14] H. Van Swygenhoven, P.M. Derlet, A. Hasnaoui, *Phys. Rev. B* 66 (2002) 024101.
- [15] H. Van Swygenhoven, P.M. Derlet, A.G. Froseth, *Acta Mater.* 54 (2006) 1975–1983.
- [16] H. Van Swygenhoven, A. Caro, *Appl. Phys. Lett.* 71 (1997) 1652–1654.
- [17] K.S. Kumar, H. Van Swygenhoven, S. Suresh, *Acta Mater.* 51 (2003) 5743–5774.
- [18] V. Yamakov, D. Wolf, S.R. Phillpot, A.K. Mukherjee, H. Gleiter, *Nat. Mater.* 3 (2004) 43–47.
- [19] S. Traiviratana, E.M. Bringa, D.H. Benson, M.A. Meyers, *Acta Mater.* 56 (2008) 3874.
- [20] M.A. Meyers, S. Traiviratana, V.A. Lubarda, D.J. Benson, E.M. Bringa, *J. Mater.* 61 (2009) 35–41.
- [21] J. Marian, J. Knap, M. Ortiz, *Phys. Rev. Lett.* 93 (2004) 165503.
- [22] J. Marian, J. Knap, M. Ortiz, *Acta Mater.* 53 (2005) 2893.
- [23] M.S. Daw, M.I. Baskes, *Phys. Rev. B* 29 (1984) 6443.
- [24] T. Mishin, M.J. Mehl, D.A. Papaconstantopoulos, A.F. Voter, J.D. Kress, *Phys. Rev. B* 63 (2001) 1.
- [25] H.N. Jarmakani, E.M. Bringa, P. Erhart, B.A. Remington, Y.M. Wang, N.Q. Vo, M.A. Meyers, *Acta Mater.* 56 (2008) 5584–5604.
- [26] X.Y. Li, Y.J. Wei, W. Yang, H.J. Gao, *Proc. Natl. Acad. Sci. USA* 106 (2009) 16108–16113.
- [27] J. Schiøtz, K.W. Jacobsen, *Science* 301 (2003) 1357–1359.
- [28] N.Q. Vo, R.S. Averback, P. Bellon, A. Caro, *Phys. Rev. B* 78 (2008) 241402.
- [29] M. Koslowski, D.W. Lee, L. Lei, *J. Mech. Phys. Solids* 59 (2011) 1427–1436.
- [30] A.M. Dongare, A.M. Rajendran, B. LaMattina, M.A. Zikry, D.W. Brenner, *Phys. Rev. B* 80 (2009) 104108.
- [31] A.M. Dongare, A.M. Rajendran, B. LaMattina, M.A. Zikry, D.W. Brenner, *J. Appl. Phys.* 108 (2010) 113518.
- [32] A.M. Guellil, J.B. Adams, *J. Mater. Res.* 7 (1992) 639–652.
- [33] M. Finnis, J. Sinclair, *Philos. Mag. A* 50 (1984) 45.
- [34] G.J. Ackland, R. Thetford, *Philos. Mag. A* 56 (1987) 15.
- [35] X.D. Dai, Y. Kong, J.H. Li, B.X. Liu, *J. Phys: Condens. Matter* 18 (2006) 4527–4542.
- [36] R.E. Rudd, *Philos. Mag.* 89 (2009) 3133–3161.
- [37] Y. Tang, E.M. Bringa, B.A. Remington, M.A. Meyers, *Acta Mater.* 59 (2010) 1354–1372.
- [38] Y. Tang, E.M. Bringa, B.A. Remington, M.A. Meyers, *APS Conf. Proc.* 1426 (2012) 1255.
- [39] K.G. Hoge, A.K. Mukherjee, *J. Mater. Sci.* 12 (1977) 1666–1672.
- [40] A. Latapie, D. Farkas, *Phys. Rev. B* 69 (2004) 134110.
- [41] D. Farkas, B. Hyde, *Nano Lett.* 5 (2005) 2403–2407.
- [42] S.L. Frederiksen, K.W. Jacobsen, J. Schiøtz, *Acta Mater.* 52 (2004) 5019–5029.
- [43] R.E. Rudd, *Mater. Sci. Forum.* 633–634 (2010) 3–19.
- [44] J.B. Jeon, B.J. Lee, Y.W. Chang, *Scr. Mater.* 64 (2011) 494–497.
- [45] Z.L. Pan, Y.H. Li, Q. Wei, *Acta Mater.* 56 (2008) 3470–3480.
- [46] S.J. Plimpton, *J. Comput. Phys.* 117 (1995) 1–19.
- [47] Z.L. Liu, L.C. Cai, X.R. Chen, F.Q. Jing, *Phys. Rev. B* 77 (2008) 024103.
- [48] H. Tsuzuki, P.S. Branicio, J.P. Rino, *Comput. Phys. Comm.* 177 (2007) 518–523.
- [49] W. Humphrey, A. Dalke, K. Schulten, *J. Mol. Graphics* 14 (1996) 33.
- [50] L.E. Murr, *Interfacial Phenomena in Metals and Alloys*, Addison-Wesley, Reading, MA, USA, 1975.
- [51] H. Gleiter, *Mater. Sci. Eng. A* 52 (1982) 91–131.
- [52] A.P. Sutton, R.W. Balluffi, *Interfaces in Crystalline Materials*, Oxford University Press, Oxford, UK, 1995.
- [53] D. Wolf, *Acta Metall.* 37 (1989) 1983–1993.
- [54] D. Wolf, *Acta Metall. Mater.* 38 (1990) 791–798.

- [55] D. Wolf, *Philos. Mag.* 62 (1990) 447–464.
- [56] R.S. Rohrer, E.A. Holm, A.D. Rollett, S.M. Foiles, J. Li, D.L. Olmsted, *Acta Mater.* 58 (2010) 5063–5069.
- [57] E.A. Holm, G.S. Rohrer, S.M. Foiles, A.D. Rollett, H.M. Miller, D.L. Olmsted, *Acta Mater.* 59 (2011) 5250–5256.
- [58] O. Voehringer, *Z. Metallkd* 11 (1972) 1119.
- [59] M.A. Meyers, C. McCowan, in: C.S. Pande, et al., (Eds.), *Interface Migration and Control of Microstructure*, ASM, Metals Park, Ohio, USA, 1986, pp. 99–124.
- [60] D. Farkas, E.M. Bringa, A. Caro, *Phys. Rev. B* 75 (2007) 184111.
- [61] S. Simões, R. Calinas, M.T. Vieira, M.F. Vieira, P.J. Ferreira, *Nanotechnology* 21 (2010) 145701.
- [62] Y. Tang, E.M. Bringa, M.A. Meyers, *Acta Mater.* 60 (2012) 4856–4865.
- [63] C. Zener, *Fracturing of Metals*, American Society for Metals, Cleveland, OH3–31.
- [64] A.N. Stroh, *Proc. R. Soc. London Ser. A* 223 (1954) 404.
- [65] E.M. Bringa, S. Traiviratana, M.A. Meyers, *Acta Mater.* 58 (2010) 4458–4477.
- [66] Y.F. Zhang, P.C. Millett, M. Tonks, B. Biner, *Scr. Mater.* 66 (2012) 117–120.
- [67] T. Dümmer, J.C. LaSalvia, G. Ravichandran, M.A. Meyers, *Acta Mater.* 46 (1998) 6267–6290.
- [68] M.A. Meyers, R.W. Armstrong, H.O.K. Kirchner, *Mechanics and Materials: Fundamentals and Linkages*, John Wiley & Sons, Inc., New York, USA489–594.
- [69] H.N. Jarmakani, B. Maddox, C.T. Wei, D. Kalantar, M.A. Meyers, *Acta Mater.* 58 (2010) 4604–4628.
- [70] H. Van Swygenhoven, J.R. Weertman, *Mater. Today* 9 (2006) 24–31.
- [71] M.F. Ashby, S.D. Hallam, *Acta Metall.* 34 (1986) 497–510.
- [72] H. Horii, S. Nemat-Nasser, *Philos. Trans. R. Soc. A* 319 (1986) 337–374.
- [73] Q. Wei, Z.L. Pan, X.L. Wu, B.E. Schuster, L.J. Kecskes, R.Z. Valiev, *Acta Mater.* 59 (2011) 2423–2436.
- [74] A. Stukowski, K. Albe, *Modelling Simul. Mater. Sci. Eng.* 18 (2010) 85001.